Modeling the thermospheric response to solar flares

David J. Pawlowski[1] and Aaron J. Ridley[1]

Received 18 March 2008; revised 30 June 2008; accepted 30 July 2008; published 24 October 2008.

[1] Measurements of the incoming solar extreme ultraviolet (EUV) irradiance now allow models to be driven at higher temporal resolution and with better accuracy than with proxy-based models. Using solar irradiance measurements from the Solar EUV Experiment (SEE) instrument to drive the Global Ionosphere-Thermosphere Model, the global thermospheric response to the 28 October 2003 and 6 November 2004 solar flares is presented. The model indicates that the thermospheric density at 400 km can increase by as much as 14.6% in under 2 hours because of the flare and takes 12 hours to settle to close to a nominal state. Intense dayside heating launches nightward propagating gravity waves that transport energy efficiently to the nightside at velocities near the local sound speed plus the bulk wind velocity. Measurements from the Champ satellite indicate that the simulated day to night propagation time is similar to the observed one. Substantial density enhancements occur near the midnight sector as the wave converges on itself. In some locations the nightside perturbations are as large as those on the dayside. The convergence of the wave also leads to significant adiabatic heating of the nightside thermosphere. Eventually, the wave is reflected back toward the dayside but is quickly damped.

Citation: Pawlowski, D. J., and A. J. Ridley (2008), Modeling the thermospheric response to solar flares, *J. Geophys. Res.*, *113*, A10309, doi:10.1029/2008JA013182.

1. Introduction

[2] Because of the ever increasing dependence on low Earth orbiting satellites, there is a need for an in-depth understanding of the dynamic processes associated with changes in solar and geomagnetic activity levels that affect the thermosphere. There are many studies in which data provided by several of the upper atmospheric and ground-based instruments have been examined in order to investigate the response of the thermosphere to dynamic conditions such as geomagnetic storms [*Hernandez et al.*, 1982; *Burnside et al.*, 1991; *Forbes et al.*, 1996; *Sutton et al.*, 2005]. These studies attempt to quantify the thermospheric perturbations that occur during dynamic time periods. In order to understand the manner in which the thermosphere can become disturbed, it is important to develop an understanding of how all different sources of dynamics can affect the atmosphere.

[3] The interaction between the solar wind and the magnetosphere is an important feature of the geospace environment that can lead to substantial perturbations in the thermosphere, especially at high latitudes. At times when the solar wind is dynamic, the magnetospheric electric field can also change quite rapidly. This electric field maps down the highly conductive magnetic field lines of the Earth into the atmosphere. At thermospheric altitudes, the ion velocity reacts almost instantly to changing electric fields. However, the neutral atmosphere is dense compared to the ionosphere, and therefore the neutral velocity reacts sluggishly to the drag force imposed by the ions. Since the ion velocity can be constantly changing, there is always a difference between the ion velocity and the neutral velocity, resulting in frictional heating which can be a very significant source of heat to the thermosphere.

[4] Another important transient feature that can result in significant perturbations to the ionosphere-thermosphere system are solar flares. Only recently have studies been performed to quantify the thermospheric response to flares using observations [*Sutton et al.*, 2006]. While this work is invaluable to the community, it is difficult to separate out the effects due to the different physical drivers, when using data or event studies. For example, when studying the thermosphere during storm time, both magnetospheric and solar forcing may contribute to the observed perturbation in the system. This is one reason why global ionosphere-thermosphere models are extremely useful [*Roble et al.*, 1988; *Fuller-Rowell and Rees*, 1980]. When using a model, it is possible to investigate the response of the atmosphere due to different forcings individually, simply by ignoring, or holding constant, other sources of dynamics. Another issue is that instruments cannot offer measurements at all scales. Ground-based instruments provide data at high temporal resolution, but at a fixed location, while space-based instruments can provide data on global scales, but the temporal resolution is restricted by the rate of precession of the satellite. Models, however, have the ability to simulate the response of the upper atmosphere to a variety of conditions, globally, and at time increments as small as the user chooses. In this study, we make use of the Global

[1]Department of Atmospheric, Oceanic and Space Sciences, University of Michigan, Ann Arbor, Michigan, USA.

0148-0227/08/2008JA013182

Ionosphere Thermosphere Model (GITM) [*Ridley et al.*, 2006] to examine the effects of solar flares on the global thermosphere.

[5] During a solar flare, the soft X-ray and parts of the extreme ultraviolet (EUV) irradiance can increase by as much as a factor of 50 in minutes [*Woods et al.*, 2004]. It is this radiation that results in the dissociation and ionization of major background atmospheric constituents, N_2, O_2, and NO. The incident photon carries much more energy than is required to dissociate or ionize the gas. In the case of dissociation, the leftover energy is used to heat the neutrals. However, it is the photoelectron, in the case of ionization, that gets the excess energy. The photoelectron is able to further ionize or dissociate the gas, and as it loses more energy, collisions with the ions begin to become important, resulting in energy transfer to the ions, and ultimately back to the neutrals [*Schunk and Nagy*, 2000].

[6] Since the thermosphere is externally driven by the solar EUV radiation, the solar flux must be specified in GITM. Historically, it has been impossible to drive a model with the exact EUV flux for a given time period because there were few measurements of that region of the solar spectrum. Instead, a proxy model is traditionally used, in which the entire EUV spectrum is related to changes in the flux measured at a specific wavelength. The 10.7 cm line has been shown to be highly correlated with solar cycle fluctuations in the EUV spectrum, and it is possible to make ground-based measurements at that wavelength [*Hinteregger et al.*, 1981; *Richards et al.*, 1994]. The availability of measurements of the solar irradiance since 2001 provides opportunities for data comparison and corrections to be made to these models [*Bailey et al.*, 2000; *Solomon et al.*, 2001; *Solomon and Qian*, 2005]. However, this $F_{10.7}$ proxy is not useful when investigating solar flares because its measurements are only available once per day.

[7] As of January 2002, measurements of the EUV spectrum have been provided by the Solar EUV Experiment (SEE) on board the TIMED spacecraft [*Woods et al.*, 1998]. SEE provides information about the solar spectrum from the soft X-ray through the EUV (.1–180 nm), using an EUV grating spectrograph (EGS) and X-ray photodiode system (XPS). SEE is constrained to rotate in one axis, which means that the sun can be in the instrument's field of view for only a few minutes each orbit. This translates to a 3% duty cycle or approximately one observation every 90 min. The ability to update the EUV irradiance every 90 min, as opposed to once per day, makes it possible to simulate the upper atmosphere under solar flare conditions and investigate the thermospheric response without making many assumptions about the nature of the solar EUV spectrum during these dynamic time periods.

[8] In this study, the SEE data are used during two flare events to drive GITM with nonvarying high-latitude conditions, allowing for the examination of the thermospheric response to flares.

2. Methodology

2.1. GITM Model

[9] The Global Ionosphere-Thermosphere Model (GITM) solves the continuity, momentum, and energy equations in three-dimensional (3-D) spherical coordinates. The coupled ionosphere-thermosphere system is solved using an altitude grid, as opposed to a pressure-based coordinate system. One of the most important features of GITM is that it does not assume hydrostatic equilibrium, which means that significant vertical flows can develop self-consistently [*Deng et al.*, 2008]. GITM is a block-based code that is entirely flexible, so the user is free to change the resolution from run to run by specifying the number of blocks to use in a given simulation. A consequence of this flexibility is that GITM can be run in one dimension where only a single latitude and longitude are simulated, and horizontal transport and gradients are ignored. Quantitative comparisons with measurements from the Millstone Hill incoherent scatter radar using both 1-D and 3-D GITM have recently been performed by *Pawlowski et al.* [2008].

[10] In GITM, the chemical source terms are included in the vertical temperature equation, which is given by

$$\frac{\partial \mathcal{T}}{\partial t} + u_r \frac{\partial \mathcal{T}}{\partial r} + (\gamma - 1)\mathcal{T}\left(\frac{2u_r}{r} + \frac{\partial u_r}{\partial r}\right) = \frac{k}{c_v \rho \overline{m}_n}\mathcal{L}, \qquad (1)$$

where $\mathcal{T} = \frac{P}{\rho}$, u_r is the vertical velocity, γ is the ratio of specific heats, k is Boltzmann's constant, c_v is the specific heat at constant volume, ρ is the mass density, P is the pressure, and $\overline{m}_n$ the average mass of the neutrals. The $\frac{k}{\overline{m}}$ on the right side of equation (1) is required to relate the normalized temperature, $\mathcal{T}$, to the thermal energy source term, $\mathcal{L}$, which is the total of the thermal energy sources, and is calculated by

$$\mathcal{L} = Q_{EUV} + Q_{NO} + Q_O + \frac{\partial}{\partial r}\left(\left(\kappa_c + \kappa_{eddy}\right)\frac{\partial T}{\partial r}\right) + N_e \frac{\overline{m}_i \overline{m}_n}{\overline{m}_i + \overline{m}_n} \nu_{in} (\mathbf{v} - \mathbf{u})^2. \qquad (2)$$

Q_{EUV}, Q_{NO}, and Q_O are the EUV heating, and NO and O cooling terms, respectively, κ_c is the thermal conductivity, κ_{eddy} is the eddy conductivity, and the final term is a frictional or Joule heating term. GITM can use a variety of methods to specify the EUV flux. Typically, the flux is based on the $F_{10.7}$ proxy as implemented by *Tobiska* [1991] and *Richards et al.* [1994]; however, GITM can also use measurements of the EUV spectrum, as is done in this study and is described in more detail below. Q_{EUV} can then be determined using ionization and heating cross sections specified by *Torr et al.* [1979]. An altitude-dependent heating efficiency is applied that is similar to the profiles described by *Torr et al.* [1980]. The radiational cooling terms are based on empirical methods described by *Kockarts* [1980] and *Kockarts and Peetermans* [1970], respectively.

[11] For this study, GITM is run at a resolution of 5° latitude × 5° longitude to simulate the flares that occurred on 28 October 2003 and 6 November 2004 and is initially run for 24 hours prior to the day of the flare to achieve a pseudo steady state. The model is then restarted at 0000 UT on the day of the flare and run twice for another 24 hours. One simulation is performed allowing only the solar flux to vary (as described below), while holding all other inputs constant, including all high-latitude forcings (the perturbed simulation). Another run is performed where

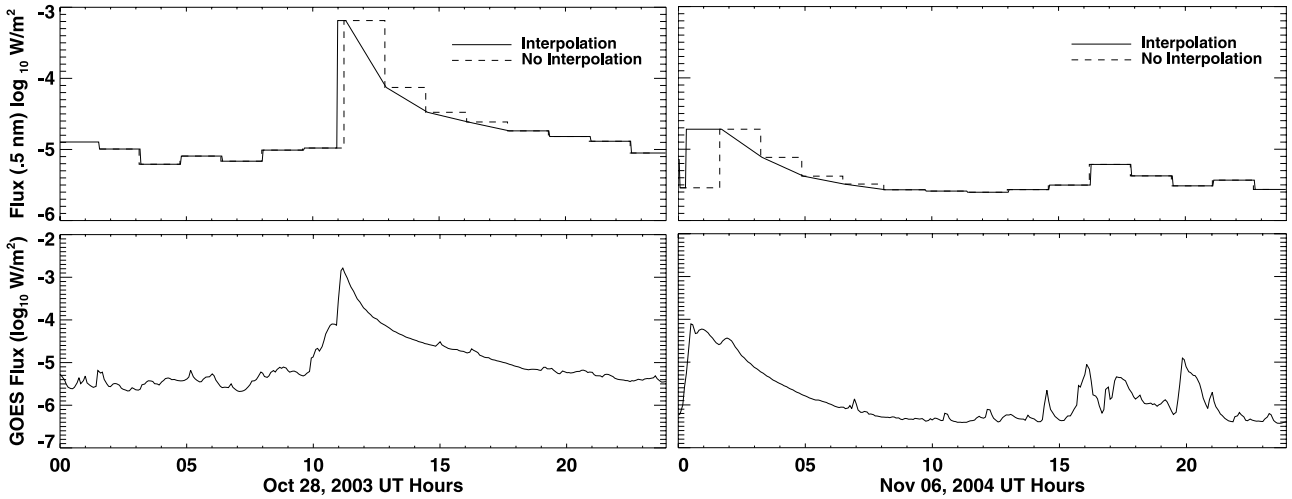

Figure 1. (top) Log_{10} solar flux at 0.5 nm on (left) 28 October 2003 and (right) 6 November 2004. The dashed line represents the flux obtained using raw SEE data. The solid line is the flux after performing an exponential interpolation during the flare and specifying the start time of the flare. (bottom) Log_{10} solar flux from GOES 1–8 angstrom channel for the same days.

the solar flux is also held constant (the unperturbed simulation) so that the runs can be compared. The perturbed and unperturbed simulations have exactly the same inputs for the first 90 min of the day. After this, the perturbed simulation's EUV flux is allowed to change. These changes are before the flare takes place, so in the results below, the differences between the simulations are nonzero at the start of the flare.

[12] In the simulations, the high latitudes are driven using the Weimer potential model [*Weimer*, 1995] and the *Fuller-Rowell and Evans* [1987] auroral precipitation model. The inputs are held constant at values that were typical of the day of each of the flares. This means that while there may be significant amounts of energy deposited into the thermosphere via the magnetosphere, this input is constant, implying that any perturbations are a result of the changing solar flux. The high latitudes may still have an effect on each individual simulation, however, because ion drag and Joule heating are taken into account, but the effects should be the same between the simulations, except for any nonlinear coupling between the constant high-latitude forcing and the effects of the solar flare.

2.2. EUV Flux

[13] In order to perform a detailed and accurate analysis of the thermospheric response to real solar flares, the model must be driven by measurements of the EUV and soft X-ray flux. One of the issues with using the SEE data to accomplish this is the instrument only has a 3% duty cycle on board TIMED, which equates to approximately one observation every 90 min. During a solar flare, *Woods et al.* [2004] shows that the soft X-rays can increase by two orders of magnitude in around 10 min. Also, typical flares last between 2 and 4 hours, which means that SEE provides only three or four measurements of the solar irradiance during a flare. Therefore, the SEE data must be interpolated. There are several different ways in which this interpolation may be performed. One such method is to make use of the X-ray data from the NOAA Geostationary Operational Environmental Satellites (GOES) [*Chamberlin et al.*, 2007]. GOES provides the X-ray flux from 0.5–4 and 1–8 Angstrom wavelength bands every minute, and thus, these data are ideal for use in performing an interpolation.

[14] A much simpler alternative to using the GOES data to interpolate the SEE data is to assume an exponential decay during the recovery of a solar flare. When GITM reaches the first SEE data point during a solar flare, the solar spectrum is then calculated during every time step for the duration of the flare using an exponential interpolation. This interpolation is calculated by determining the decay rate between the two closest data points surrounding the current time in the simulation, and utilizing that rate to calculate the flux at the current time. This method does not require any knowledge of how the EUV wavelengths correlate to the X-rays, as is the case when using the GOES X-ray data as a proxy. The only remaining issue is that owing to the sparsity of the SEE data, there may be significant error in specifying when the flare begins. Since SEE observations are made every 90 min, it is possible that the timing of the flare is off by as much as 90 min. Therefore, it is necessary to use the GOES data to determine the start time of the flare. The top panels in Figure 1 show the solar flux at .5 nm calculated using the SEE measurements on 28 October 2003 (left) and 6 November 2004 (right). The dashed line shows the flux that would drive the model if only the raw SEE data are used without any interpolation. If the start time of the flare is specified in GITM using the GOES data (bottom of Figure 1), and an exponential interpolation is performed between SEE data points, the solid line is obtained. By specifying the start time, GITM will simulate the October flare about 20 min before it would otherwise, and the November flare, an hour and a half earlier. After approximately 6 hours, the SEE data are no longer interpolated.

[15] One possible source of error in using the SEE data is due to the approximate 10% uncertainty in energy input given by the instrument [*Woods et al.*, 1998]. This may lead to a errors in both the temporal dynamics and strength of the

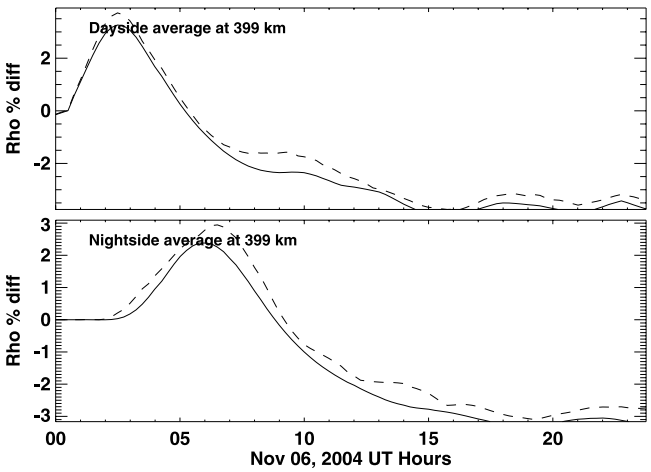

Figure 2. Difference plots of the thermospheric density on 6 November 2004. The dayside average (solid lines) and dayside maximum differences (dashed lines) are plotted at 400 km in the top panel and nightside values at the same altitude are shown in the bottom panel.

thermospheric model reaction to the solar flare. In addition, no assumptions are made about the solar flux prior to the first SEE measurement during the flare. Rather, the study uses a very conservative approach to interpolating the SEE data. When the simulated time reaches the start time of the flare, the EUV flux increases to the value obtained from the first SEE measurement during the flare, even though the actual flux is almost certainly larger, since the measurement is in the future. This is the case for both the 28 October event, where the first SEE measurement of the flare is only a few minutes after the actual start of the event, and the 6 November event, where the first SEE measurement is nearly an hour and a half after the actual start of the flare. While simulating both events in this manner will lead to an underestimation of the incident energy into the thermosphere, the amount of energy missed during the November event is likely much larger than the energy missed during the October event due to the timing of the SEE measurements. However, the goal of this study is not to determine the exact thermospheric perturbation during a specific solar flare, but rather to obtain insight into how the thermosphere responds globally, so this underestimation is acceptable. A brief comparison of the model results with data from the Champ satellite, which is described by *Reigber et al.* [2000], is presented in section 3.3; however, the studies by *Sutton et al.* [2006] and *Liu et al.* [2007] attempt to accurately quantify the density response during the October 2003 flare using in situ accelerometer data.

3. Results

3.1. Day and Night Perturbation

[16] Figures 2 and 3 show difference plots between the perturbed and unperturbed simulations on 28 October 2003 and 6 November 2004, respectively. Here, we define the dayside as being solar zenith angles (SZAs) less than 30°, while the nightside is defined as SZAs larger than 150°. The average dayside and nightside density percent difference, which is calculated by

$$\rho\%_{diff} = \frac{\rho_{perturbed} - \rho_{unperturbed}}{\rho_{unperturbed}}$$

along with the maximum percent difference in each region, are plotted at 110 and 400 km (400 km only for 6 November 2004). Also shown are the corresponding average vertical velocities at 400 km for 28 October 2003.

[17] The November flare was significantly smaller than the October flare, and therefore the response was considerably weaker. For the 6 November flare, the maximum difference on the dayside at 110 km (not plotted) is less than 0.15% and on the nightside, an order of magnitude weaker. At 400 km, the maximum response is more substantial, 3.7% on the dayside, and 3.0% on the nightside, but still much smaller than the reaction during the October event. Since the trends in the results for both 28 October 2003 and 4 November 2004 are very similar, the focus here will be on the October simulation.

[18] During the 28 October 2003 event (Figure 3), on the dayside, the density response at 110 km is again quite small. The largest average density perturbation is less than 0.2%. The maximum difference reaches 2.9%, but it does so several hours after the flare occurs. This perturbation is at the forward edge of a traveling disturbance that propagates toward high latitudes before diffusing away. The perturbation is extremely localized, only extending 20° in latitude, and it is traveling at an average speed of 310 m/s (± 50 m/s). There is a sharp neutral wind gradient at the leading edge of the disturbance which results in a buildup of density. Figure 3 indicates that the density enhancement begins to decrease after 1700 UT. This is the case because the wave is moving out of the SZA < 30° region, not because the disturbance itself is becoming weaker. Rather, it continues propagating toward the northern high latitudes and the density enhancement reaches a maximum of 5.2% at a SZA of 62°, at 1915 UT, before slowing owing to the presence of oppositely directed winds. As the disturbance slows, it quickly diffuses away.

[19] At 400 km, the thermosphere begins to react to the flare within 15 min, but the maximum dayside perturbation does not occur until over an hour and a half later. Before the flare occurs, the density difference is actually negative. This is because the EUV flux just prior to flare used in the perturbed simulation was actually smaller than the constant value used for the unperturbed simulation. At 1245 UT, the maximum difference between the perturbed and unperturbed runs is 14.9% and the average difference is 13.6%. The thermosphere on the dayside starts to recover, taking approximately 5 hours until the average density at this altitude reaches a local minimum (1800 UT) before slightly increasing again. There is then a small secondary maximum that occurs at about 2030 UT at 400 km.

[20] The vertical winds at 400 km are also highly perturbed. The wind percent difference, which is calculated in the same manner as the density percent difference, reaches a maximum increase of 400% (13 m/s) compared to the unperturbed simulation at 1115 UT. This wind disturbance is not localized, but rather encompasses the entire dayside. As the thermosphere absorbs the excess solar energy, the

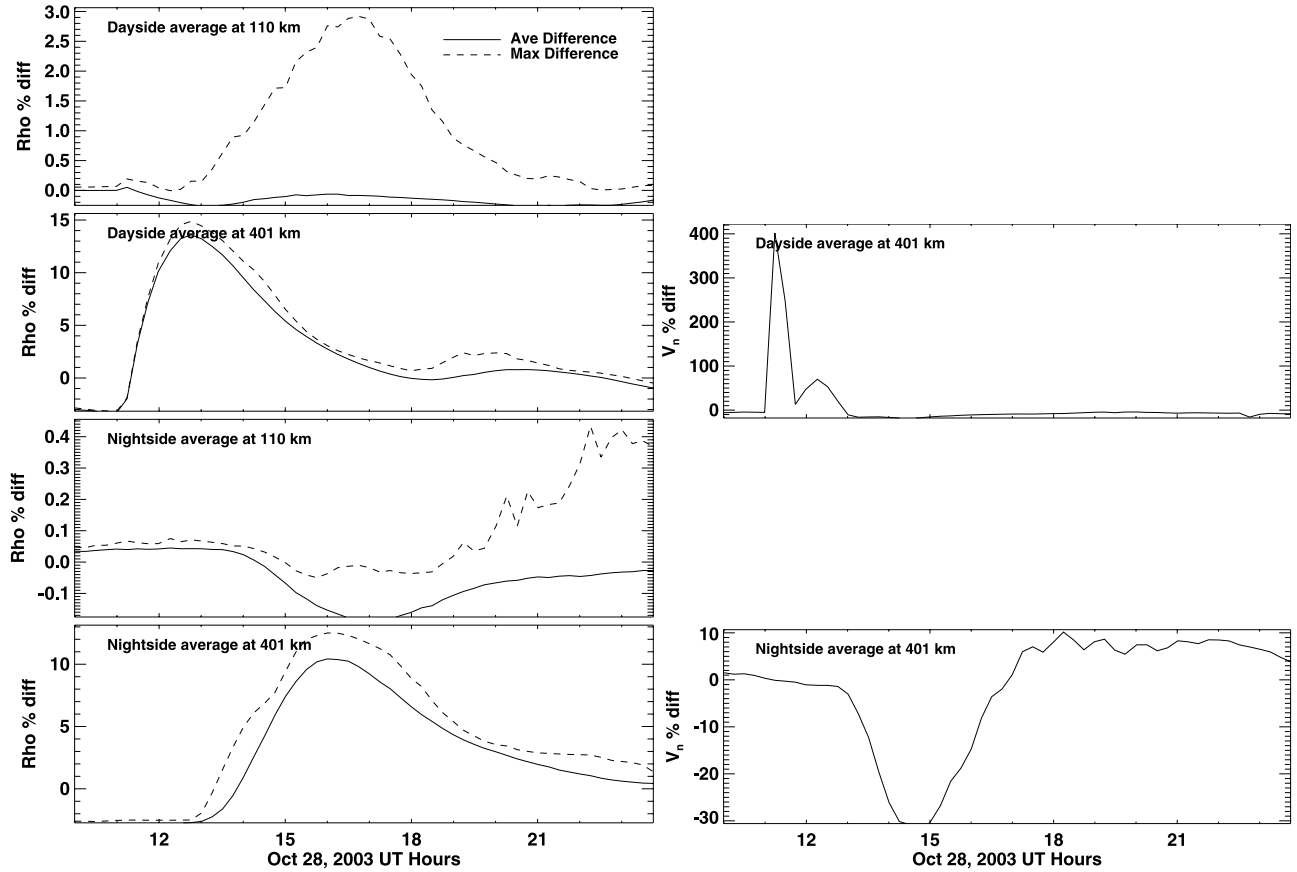

Figure 3. Similar to Figure 2 except for the 28 October 2003 flare. Density results are also shown at 110 km. Also, the vertical velocity differences are shown on the right, only at 400 km.

entire atmosphere expands, and thus the average vertical velocity is highly perturbed. This is a hydrostatic expansion of the atmosphere, synonymous with an increase in the height of pressure levels. By 1300 UT, the winds have died down, and the perturbation is slightly negative for most of the remainder of the day.

[21] On the nightside, there is no significant response at 110 km, since the propagation of the small disturbance stalls in the high latitudes; however, there is a substantial reaction at 400 km. The density enhancement on the nightside at 400 km is nearly as large as that on the dayside. The maximum density difference of 12.5% occurs at 1615 UT. The maximum average difference reaches 10.4% half an hour earlier. This indicates that there is a traveling disturbance that reaches the nightside thermosphere, and that the nightward propagation is highly efficient. Similarly to the density response at 110 km on the dayside, the largest nightside density perturbation at 400 km does not occur at a SZA >150°. At 1630 UT, SZA = 124°, there is a maximum difference of 13.4%. This maximum occurs as a result of the convergence of wind flows between the equatorial and the high-latitude regions due, in part, to the high-latitude inputs used in the simulation. This means that the location of the maximum is a consequence of this particular time period, and not necessarily indicative of every solar flare event.

[22] The addition of energy to the thermosphere should have an observable effect on the temperature as well as the density. Figure 4 shows the temperature perturbations in the same manner as Figure 3. At 110 km on the dayside, the maximum temperature perturbation is 3.0%, or 10 K, at 1600 UT. This maximum is a result of the traveling disturbance encountering slow winds, as described above, leading to adiabatic heating of the gas, and not due directly to the increase in energy absorption. At 400 km the temperature increases on most of the dayside, resulting in a maximum average perturbation of 3.4% (1257 K for the perturbed simulation versus 1212 K for the unperturbed simulation). On the nightside, at 400 km, the magnitude of the temperature perturbation is similar to that on the dayside. This is due to adiabatic heating of the gas as the nightward propagating wave converges on itself. The temperature perturbation at 110 km is significantly less.

3.2. Wave Propagation

[23] Figure 5 shows the percent difference of density averaged over 7.5° solar zenith angle bins for 8 different altitudes. At each altitude, solar zenith angle profiles are plotted corresponding to nine different times, separated by 15 min, beginning at 1115 UT and ending at 1315 UT. In the figure, it is possible to see the propagation of the disturbance from low to high solar zenith angles. Just after the flare occurs (black line), the density has begun to increase at all altitudes. At 110 km, the density difference is a maximum at this time (as mentioned above, the density percent difference is negative because the unperturbed simulation

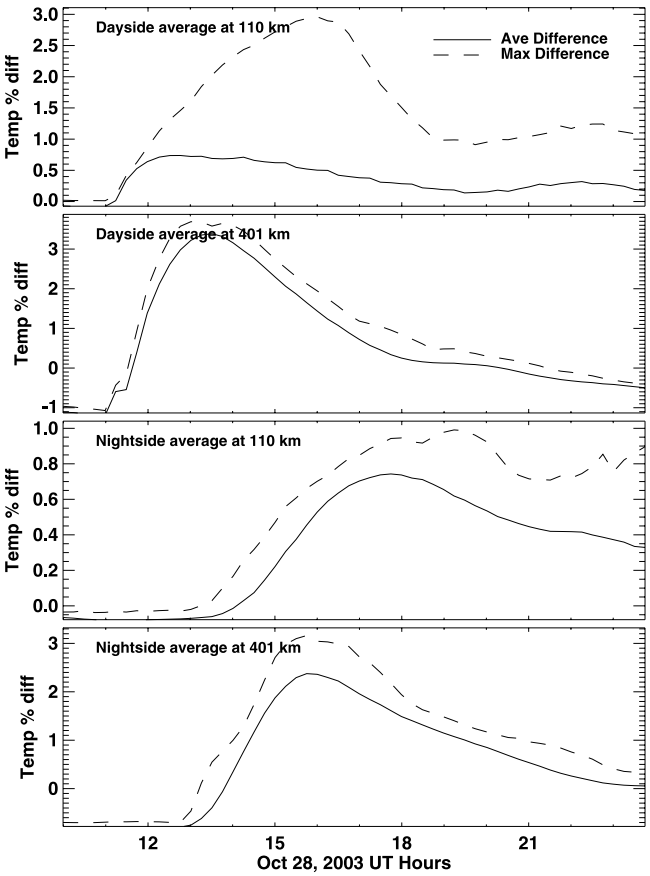

Figure 4. Difference plots from GITM simulations of the thermospheric temperature on 28 October 2003. The dayside average (solid lines) and dayside maximum differences (dashed lines) are plotted in the top two panels at 110 km and 400 km, respectively. Nightside values at the same altitudes are shown in the bottom two panels.

was run using the first SEE measurement of the day, which is larger than the measurement just before the flare). At higher altitudes, the atmosphere has just begun to change. As time progresses (from purple to red lines), the disturbance extends to higher and higher solar zenith angle. At 400 km, the wave propagates all the way to SZA = 175° by 1330 UT.

[24] Figure 5 indicates that the propagation of the disturbance is very dependent on altitude. At lower altitudes, the thermosphere responds much more directly to the change in the solar flux. Figure 3 shows that the response at 110 km, while small, is directly driven by the changing incident energy. This means that the maximum density perturbation is expected to occur very near the time of the maximum incident solar flux, as is the case here. Since the sun shines on the entire dayside, and not only the subsolar location, the flare has a direct effect between 0° and 90° SZA at all altitudes. A consequence of this is that the peak density perturbation immediately after the flare is not necessarily confined to near the subsolar point. This is especially the case at intermediate altitudes.

[25] Above about 200 km, the density perturbation reaches midnight, while below 200 km it does not. At 400 km, the wave travels from SZA = 100° to SZA = 165° in about 2 hours. This means that the day to night propagation speed is approximately 1070 m/s (±150 m/s due to 15 min temporal resolution of the results and the spatial resolution used in the model). At 400 km, the global mean sound speed is 910 m/s. The average day to night neutral wind speed due to dayside heating is, on average, between 100 and 200 m/s, depending on latitude and solar zenith angle. This indicates that the wave is most likely moving at a velocity that is approximately equal to the bulk wind velocity plus the sound speed.

[26] At 15:45 the wave has propagated completely to the midnight sector. Figure 6 shows the same type of plot as Figure 5, but for only 401 km altitude and from 1545–1845 UT. At 1545 UT, the perturbation is reflected back toward the dayside. However, the disturbance travels at an average speed of 575 m/s (± 90 m/s), much slower than it did when moving from day to night. This speed is slightly slower than the bulk wind speed plus the sound speed (i.e., 910 − 200 m/s = 710 m/s), but is relatively close, given the uncertainty, and the fact that the nightside sound speed may be slightly lower than the global sound speed, owing to the temperature being lower. As a consequence, the perturbation mostly diffuses away before it returns to the dayside.

3.3. Comparison with Champ

[27] The availability of mass density data from the Champ satellite, which is in a polar orbit at approximately 400 km, provides an opportunity for observational support of the features described above. Figure 7 shows a direct comparison between the Champ data (top) and GITM results from the perturbed simulation (bottom), where the dayside (left) and nightside densities are plotted as a function of latitude and universal time. It is important to point out that no attempt to remove the density fluctuations in the Champ data due to external forcings other than the solar EUV has been made. This means that while the GITM results show only perturbations due to the changing solar flux, the Champ densities are significantly effected by high-latitude dynamics. This issue is demonstrated in the right side of Figure 7, where the Champ observations show an equatorward propagating disturbance that is launched from the southern high latitudes around 0700 UT. The GITM results on the other hand, show no such disturbance. This makes comparison of data and model particularly difficult. Still, it is possible to make quantitative comparisons of several features.

[28] On the dayside, Champ observations indicate two local maxima after the flare begins. While GITM does not capture the second maxima, the first one does show up in the simulation results. At 1254 UT, GITM reaches a maximum value of 16.39×10^{-12} km/m^3 at 2°S latitude while the Champ observations indicate a local maximum at 1254 UT and 6°S latitude of 15.38×10^{-12} km/m^3. This means that while the observed peak occurs one GITM cell southward of the simulated one, the time at which it occurs in the model is quite precise. The magnitude of the GITM maximum is larger than that of Champ; however, the increase over the average pre-flare values at the same

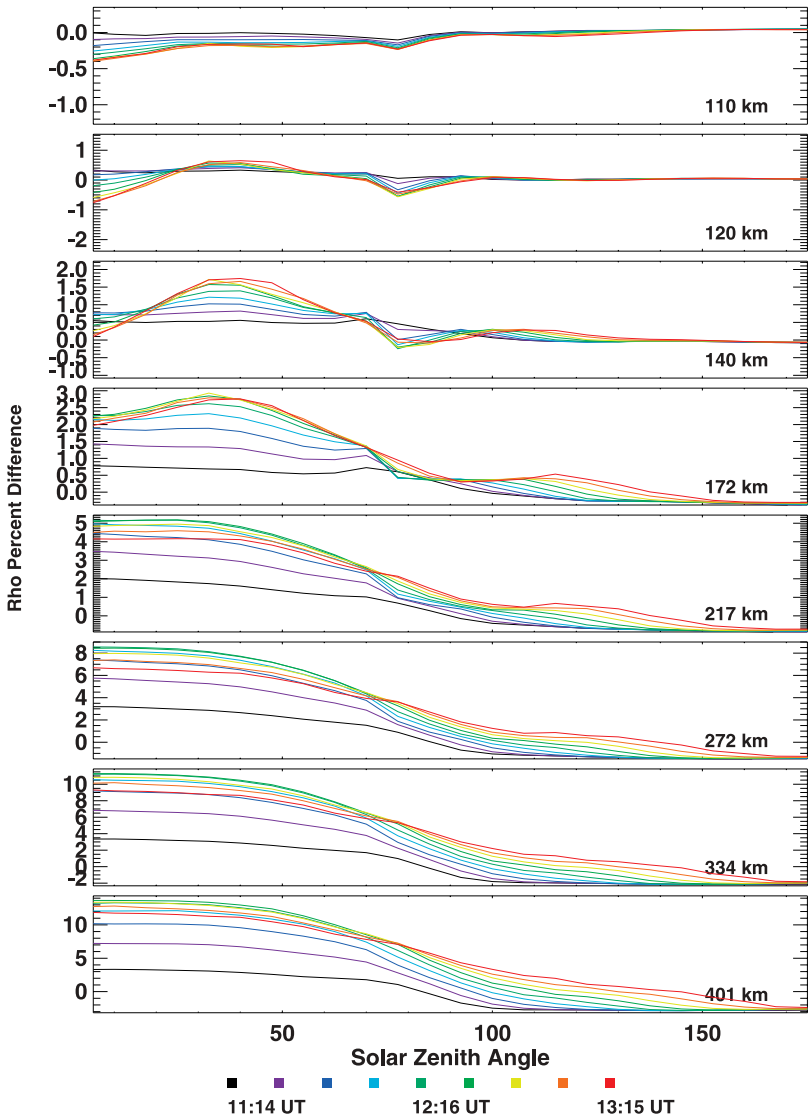

Figure 5. Density percent difference versus solar zenith angle at 8 altitudes. Profiles are plotted at 9 different times separated by 15 min, beginning at 1115 UT.

latitude of the maximum is 45.7% for Champ compared to only 14.1% for GITM.

[29] Although the time at which GITM and Champ reach the local maximum values is the same, the Champ densities begin to increase nearly an hour before the GITM densities. This is due to the conservative approach used to specify the EUV flux within GITM. Prior to the flare, GOES indicates an increase in the soft X-ray flux beginning around 1000 UT. A similar increase does not show up in the SEE data because the last measurement prior to the flare was taken at 0940 UT. In this case, there is some ambiguity as to when the flare actually begins. Here, it is specified to begin when the GOES flux gradient is sharpest, which is after 1100 UT,

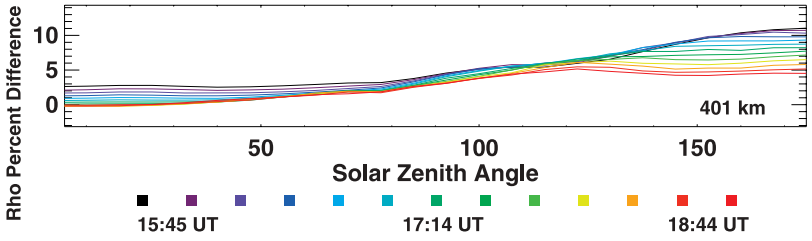

Figure 6. Similar to Figure 5, beginning at 1545 UT and ending at 1845 UT only at 400 km.

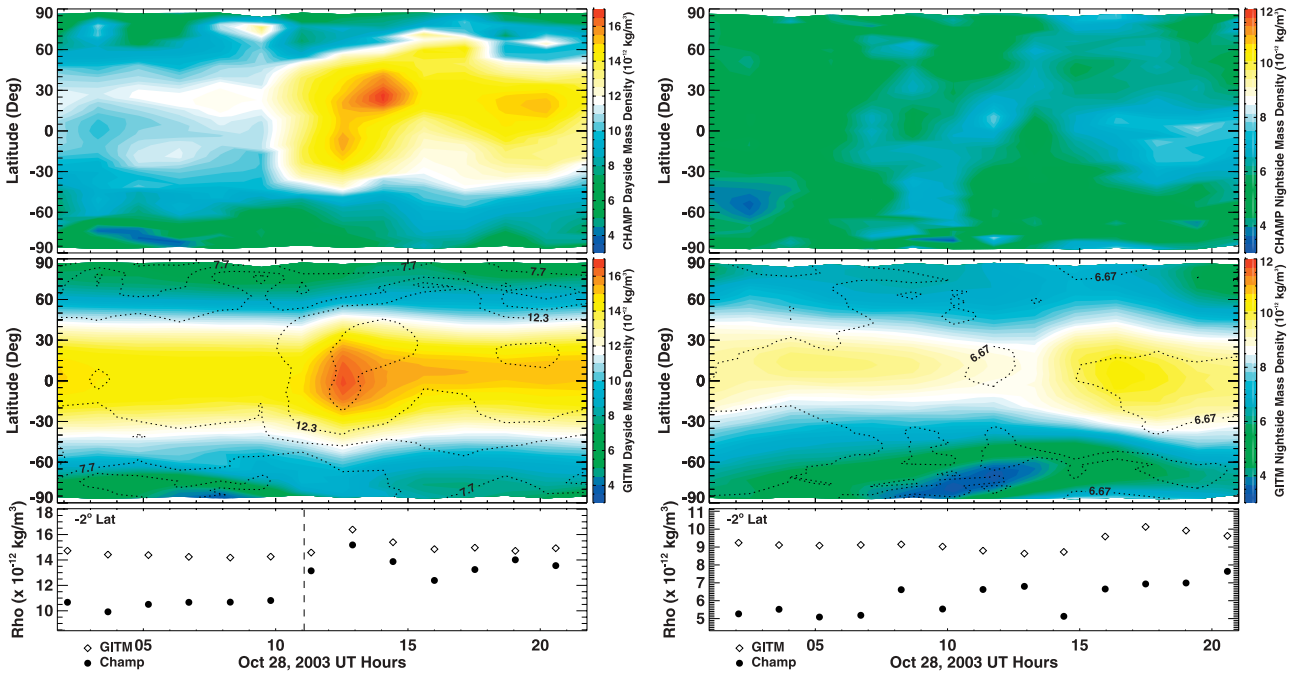

Figure 7. Contour plots of neutral density (top) from the Champ satellite and (middle) from GITM, extracted at the location of the satellite, as well as (bottom) a scatterplot of density results at 2°S latitude from both Champ and GITM. The dayside values (~1320 local time (LT)) are plotted on the left, and the nightside values (~0120 LT) are plotted on the right. The dashed lines in the 2-D plots are contours of the Champ data plotted on top of the GITM results for comparison. The start time of the flare is indicated by a vertical dashed line.

and thus the smaller flux increase that occurs prior to the flare is not captured by the model.

[30] On the nightside, Champ indicates much more structure in the densities than does GITM. As mentioned, there are obvious high-latitude disturbances in the data affecting the midlatitudes and low latitudes that begin before the flare starts. In addition, the background winds play a significant role in determining the location, time, and magnitude of any nightside perturbations caused by traveling disturbances. For these reasons there is increased uncertainty in making comparisons between observations and model on the nightside. Regardless, both model and data do show a slight sudden increase in the densities beginning around 1400 UT which maximizes in GITM at 1646 UT. In the Champ data, the density increase is observed as a light blue region between ±25° latitude starting between 1400 and 1500 UT. In the GITM plot, the background density is much larger, so the response may be harder to see, although there is a general decrease in the density from about 0900 UT until the perturbation arrives on the nightside, which the GITM plot shows to occur around 1400 UT. This is much easier to see in the bottom plots which show the values at −2° latitude. The model indicates that this increase, averaged over ±25° latitude for 3 hours is 15.3% compared to 20.5% as observed by Champ. This density enhancement in GITM corresponds to the arrival of the nightward propagating gravity wave in the midnight sector. It is outside the scope of this study to determine the relative importance of nightward propagating gravity waves launched by solar inputs versus traveling disturbances initiated by high-latitude heating on the enhancement seen by Champ. However, the timing and the magnitude of the disturbance suggests that this feature is at least in part influenced by solar effects on the thermosphere.

4. Discussion and Conclusions

[31] GITM shows that the thermosphere can be highly effected by solar flares on both the dayside and the nightside. While the focus of this study has been on the 28 October 2003 event, the characteristics of the thermospheric response were similar for both the 28 October event and the 6 November 2003 event. At 110 km, the model indicates that the atmospheric mass density at the subsolar location is not significantly perturbed. This is an expected result. During a solar flare, the shorter EUV wavelengths are enhanced the most. The solar flux at soft X-ray and EUV wavelengths is severely perturbed during strong flares. As a consequence of the exponential decrease of the neutral density with height, the altitude at which most of the photoabsorption occurs is where the optical depth:

$$\tau(\lambda, \chi, z) = \sum_i \sigma_i(\lambda) n_i H_i Ch(\chi, z) \tag{3}$$

is equal to unity [*Kockarts*, 1981]. Here, χ is the solar zenith angle, $\sigma_i(\lambda)$ the absorption cross section at wavelength λ for the species i with density n_i, and scale height H_i at altitude z, and $Ch(\chi, z)$ is the Chapman function. Figure 8 shows the altitude at which unit optical depth is reached for wavelengths between 10 and 700 angstroms on 28 October 2003 at 1200 local time at the

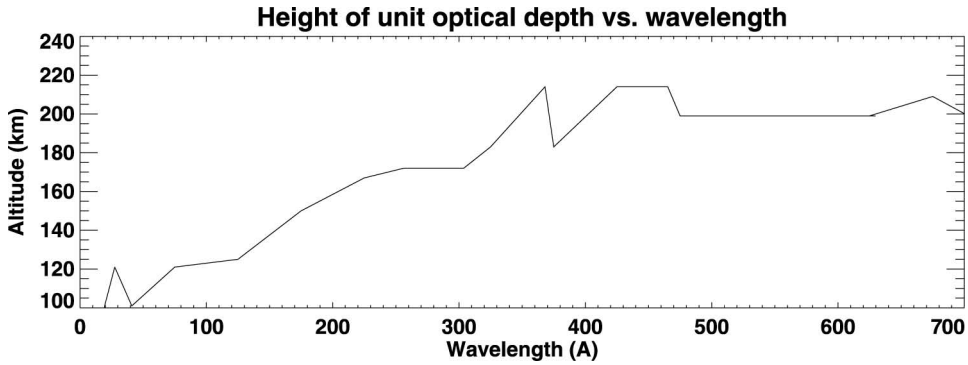

Figure 8. Altitude of unit optical depth versus wavelength for 28 October 2003 at 1200 local time at the equator.

equator, as calculated by GITM. The majority of the energy in this region of the spectrum is absorbed from about 120 to nearly 200 km. The density perturbation at a specific altitude is primarily caused by heating below this altitude, so if there is little heating below, the density will not be significantly affected. This means that during a flare, one would not expect a significant density response to occur below 120 km. Near 120 km, where most of the dynamic wavelengths deposit their energy, the thermosphere begins to have a more substantial response. Above 200 km, the atmosphere is so rarefied that efficient absorption of the solar radiation is minimal, and thus the temperature is not directly affected by the flare. However, as energy is absorbed lower in the atmosphere, the entire thermosphere hydrostatically expands, resulting in enhanced upward directed vertical winds (Figure 3, right) that bring higher density air up from the lower thermosphere. At 400 km, the integral effect also plays a substantial role on the density perturbation. At higher altitudes, the local density is a function of the density at all lower altitudes. Therefore, if the density is perturbed below 400 km, the density at 400 km will be effected.

[32] In addition to significant density perturbations at 400 km, the thermospheric temperature is also disturbed. Figure 9 shows the dayside average temperature difference as a function of altitude at 1200 and 1300 UT, and indicates that conduction plays a role in heating the thermosphere at higher altitudes. During the flare, the lower thermosphere is heated the most, since the extra energy is mostly absorbed there, as indicated in Figure 8. Owing to this additional energy, less heat is conducted down from higher altitudes, and since the density is so much lower higher up, the extra heat has a substantial effect on the temperature. Therefore, dayside heating of the thermosphere above 200 km during solar flares is primarily due to reduced downward conduction.

[33] One of the most interesting features of the modeled response is the magnitude of the nightside density perturbation at high altitudes. On the 28th, the maximum nightside response at 400 km is only slightly smaller than the maximum dayside perturbation. This disturbance propagates from the dayside to the nightside at a speed of approximately 1070 m/s, which is close to the local sound speed at 400 km plus the bulk neutral wind velocity. On the nightside, the magnitude of the perturbation is not only a result of upward directed flows. In fact, the vertical flows are enhanced downward until 1600 UT, even though the density perturbation is growing during this time. Rather, the density increase is primarily due to the traveling disturbance converging on itself as it passes through the dawn and dusk sectors and over both poles. This also results in significant adiabatic heating of the gas. Evidence of this is observed in the temperature plots (Figure 4), where there is a significant temperature perturbation on the nightside at 400 km that corresponds, very closely, with the density perturbation.

[34] It may be expected that this nightside maximum would occur very close to the antisunward point (SZA = 180°); however, as mentioned, the largest perturbation occurs at a SZA of 124°. This is primarily due to the global distribution of neutral winds that act to steer the disturbance. Figure 10 shows a time series of the thermospheric density difference at 400 km beginning at 1400 UT and ending at 2015 UT with the neutral wind vectors (nondifferenced) overplotted. The plots are spaced in time by 45 min. As the wave travels toward the nightside, the strong equatorward directed flows determine the location of the maximum convergence. In this simulation, steady high-latitude inputs were used that were characteristic of those on 28 October. These inputs drive ion flows that enhance the neutral winds. This source of momentum along with the Coriolis force serve to make the wave not converge at exactly 180° SZA.

[35] The largest dayside density perturbation at 110 km occurs in the northern high latitudes, far from the subsolar

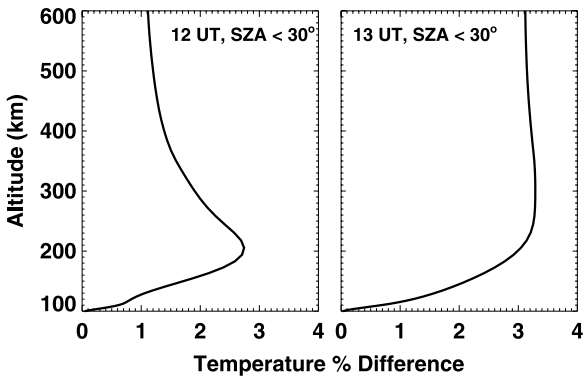

Figure 9. Altitude profile of the average dayside (SZA < 30°) thermospheric temperature difference between the perturbed and unperturbed simulations at (left) 1200 UT and (right) 1300 UT.

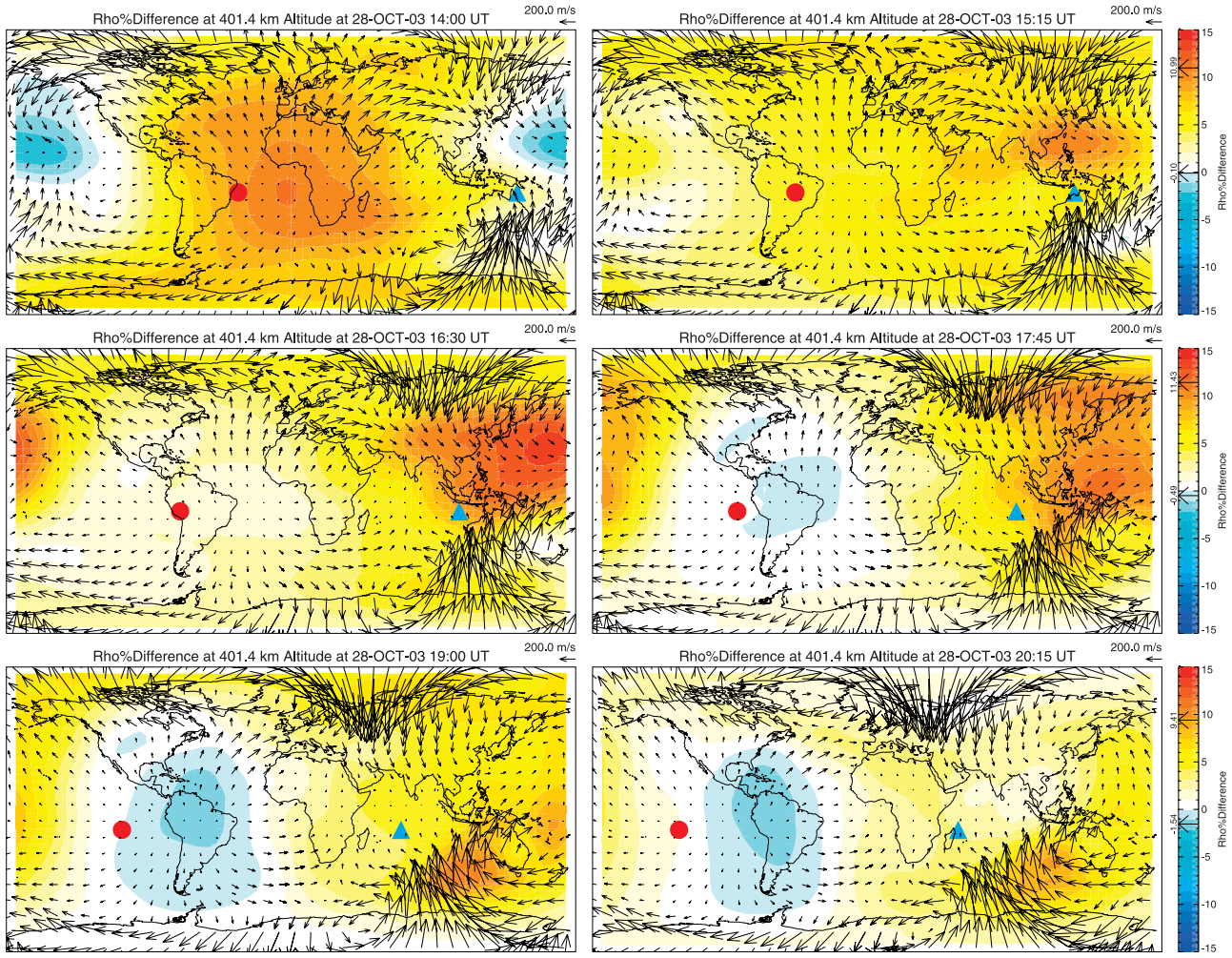

Figure 10. Difference contours of thermospheric density at 400 km beginning at 1400 UT and ending at 2015 UT. The neutral wind vectors from the perturbed simulation are overplotted. The red circle and the blue triangle indicate the subsolar point and antisolar point, respectively.

point (not plotted). The density perturbation is a result of air from the high density subsolar region being pulled northward by neutral winds that are significantly enhanced by ion drag. In front of the leading edge of this disturbance, the winds are significantly weaker and eastward, which is perpendicular to the northward directed flow that is carrying the disturbance. This strong wind gradient causes a pile up of neutral gas as the disturbance moves northward. As the wave moves into the midlatitudes and high latitudes, the density perturbation continues to grow. As the wave passes the terminator, however, it encounters mostly oppositely directed neutral winds. This causes the wave to quickly slow and diffuse away.

[36] Another interesting feature of the results is that there is a significant difference between the day to night propagation speed, and the speed of the disturbance once it is reflected back toward the dayside. The reason for this is demonstrated in Figure 10. At all times, the global circulation pattern is dominated by pressure gradients that are set up by solar heating. Prior to 1630, the time at which the maximum perturbation occurs on the nightside, the disturbance is spreading around the globe such that the direction of propagation is in the direction of the neutral winds, antisunward. After 16:30, the wave begins traveling back toward the dayside. When the disturbance is reflected, and starts propagating sunward, the wave encounters oppositely directed winds, which act to slow the propagation. As the disturbance is slowed, it can easily diffuse away, and therefore, is unable to completely propagate back to the dayside. Remnants of the wave show up in the SZA $< 30^{\circ}$ region which causes a small secondary maximum around 2030 UT. By 2300 UT, the largest perturbation in the thermospheric density at 400 km is below 5%.

[37] The results suggest that the day to night propagation speed is approximately equal to the sum of the bulk wind speed and the local sound speed. This is also the case for the reflected wave; however, the high-latitude winds have a more significant influence on the reflected wave than the nightward propagating wave, since the effects of the high-latitude drivers extend deep into the midlatitude region. This means the bulk velocity, on average, is larger (in the opposite direction) for the reflected wave. Also, the high-latitude wind patterns on the nightside are much less isotropic than the pressure gradient induced winds on the

dayside. Therefore, the reflected wave speed is much more dependent on location.

[38] This work shows that the solar flares can have a significant effect on the entire global thermosphere, and not just the dayside. Heating and atmospheric expansion on the dayside can cause disturbances at all altitudes, and can lead to the propagation of a large-scale gravity wave that travels near the local sound speed plus the bulk neutral wind velocity and, at higher altitudes, efficiently transports energy to the nightside. The thermosphere may then experience significant nightside density enhancements and be subject to adiabatic heating as the wave converges on itself (4–5 hours after the flare). While the trends in the thermospheric response are similar for both events presented in this study, this does not mean that all flare events have the same effect on the thermosphere. This study indicates that interesting physics can occur, and while a brief comparison with data from the Champ satellite indicates that structures exist on the nightside that may be related to gravity waves propagating from the dayside, future work in this research requires a more statistical analysis using both data and model so detailed observational support for these global-scale effects can be provided.

[39] **Acknowledgments.** SEE data were obtained from the TIMED/SEE data archive at http://lasp.colorado.edu/see/see_data.html. The authors would like to thank Tom Woods, the PI for the SEE instrument, for making these data available. GOES data were obtained from http://www.ngdc.noaa.gov/stp/GOES/goes.html. Champ data (version 2.0) were provided by Eric Sutton http://sisko.colorado.edu/sutton/data.html. This study was supported in part by NSF grants 0539053 and ATM0639336 and AFOSR grant FA9550-07-1-0434.

[40] Zuyin Pu thanks Thomas Woods and another reviewer for their assistance in evaluating this paper.

References

Bailey, S. M., T. N. Woods, C. A. Barth, S. C. Solomon, L. R. Canfield, and R. Korde (2000), Measurements of the solar soft X-ray irradiance by the Student Nitric Oxide Explorer: First analysis and underflight calibrations, *J. Geophys. Res.*, *105*, 27,179–27,194, doi:10.1029/2000JA000188.

Burnside, R. G., C. A. Tepley, M. P. Sulzer, T. J. Fuller-Rowell, and D. G. Torr (1991), The neutral thermosphere at Arecibo during geomagnetic storms, *J. Geophys. Res.*, *96*, 1289–1301.

Chamberlin, P. C., T. N. Woods, and F. G. Eparvier (2007), Flare Irradiance Spectral Model (FISM): Daily component algorithms and results, *Space Weather*, *5*, S07005, doi:10.1029/2007SW000316.

Deng, Y., A. D. Richmond, A. J. Ridley, and H.-L. Liu (2008), Assessment of the non-hydrostatic effect on the upper atmosphere using a general circulation model (GCM), *Geophys. Res. Lett.*, *35*, L01104, doi:10.1029/2007GL032182.

Forbes, J. M., R. Gonzalez, F. A. Marcos, D. Revelle, and H. Parish (1996), Magnetic storm response of lower thermosphere density, *J. Geophys. Res.*, *101*, 2313–2320, doi:10.1029/95JA02721.

Fuller-Rowell, T. J., and D. Evans (1987), Height-integrated Pedersen and Hall conductivity patterns inferred from TIROS-NOAA satellite data, *J. Geophys. Res.*, *92*, 7606.

Fuller-Rowell, T. J., and D. Rees (1980), A three-dimensional, time-dependent, global model of the thermosphere, *J. Atmos. Sci.*, *37*, 2545.

Hernandez, G., R. G. Roble, E. C. Ridley, and J. H. Allen (1982), Thermospheric response observed over Fritz Peak, Colorado, during two large geomagnetic storms near solar cycle maximum, *J. Geophys. Res.*, *87*, 9181–9192.

Hinteregger, H. E., K. Fukui, and B. R. Gibson (1981), Observational, reference and model data on solar EUV from measurements on AE-E, *Geophys. Res. Lett.*, *8*, 1147.

Kockarts, G. (1980), Nitric oxide cooling in the terrestrial thermosphere, *Geophys. Res. Lett.*, *7*, 137.

Kockarts, G. (1981), Effects of solar variations on the upper atmosphere, *Sol. Phys.*, *74*, 295–320.

Kockarts, G., and W. Peetermans (1970), Atomic oxygen infrared emission in the Earth's upper atmosphere, *Planet. Space Sci.*, *18*, 271.

Liu, H., H. Lühr, S. Watanabe, W. Köhler, and C. Manoj (2007), Contrasting behavior of the thermosphere and ionosphere in response to the 28 October 2003 solar flare, *J. Geophys. Res.*, *112*, A07305, doi:10.1029/2007JA012313.

Pawlowski, D. J., A. J. Ridley, I. Kim, and D. S. Bernstein (2008), Global model comparison with Millstone Hill during September 2005, *J. Geophys. Res.*, *113*, A01312, doi:10.1029/2007JA012390.

Reigber, C., H. Luhr, and P. Schwintzer (2000), CHAMP mission status and perspectives, *Eos Trans. AGU*, *81*(48), Fall Meet. Suppl., Abstract G52A-01.

Richards, P. G., J. A. Fennelly, and D. G. Torr (1994), EUVAC: A solar EUV flux model for aeronomic calculations, *J. Geophys. Res.*, *99*, 8981.

Ridley, A. J., Y. Deng, and G. Toth (2006), The global ionosphere-thermosphere model, *J. Atmos. Sol. Terr. Phys.*, *68*, 839.

Roble, R. G., E. C. Ridley, A. D. Richmond, and R. E. Dickinson (1988), A coupled thermosphere/ionosphere general circulation model, *Geophys. Res. Lett.*, *15*, 1325.

Schunk, R. W., and A. F. Nagy (2000), *Ionospheres*, Cambridge Univ. Press, Cambridge, U. K.

Solomon, S. C., and L. Qian (2005), Solar extreme-ultraviolet irradiance for general circulation models, *J. Geophys. Res.*, *110*, A10306, doi:10.1029/2005JA011160.

Solomon, S. C., S. M. Bailey, and T. N. Woods (2001), Effect of solar soft X-rays on the lower ionosphere, *Geophys. Res. Lett.*, *28*, 2149.

Sutton, E. K., J. M. Forbes, and R. S. Nerem (2005), Global thermospheric neutral density and wind response to the severe 2003 geomagnetic storms from CHAMP accelerometer data, *J. Geophys. Res.*, *110*, A09S40, doi:10.1029/2004JA010985.

Sutton, E. K., J. M. Forbes, R. S. Nerem, and T. N. Woods (2006), Neutral density response to the solar flares of October and November, 2003, *Geophys. Res. Lett.*, *33*, L22101, doi:10.1029/2006GL027737.

Tobiska, W. K. (1991), Revised solar extreme ultraviolet flux model, *J. Atmos. Terr. Phys.*, *53*, 1005.

Torr, D. G., et al. (1979), An experimental and theoretical study of the mean diurnal variation of O^+, NO^+, O_2^+, and N_2^+ ions in the mid-latitude F_1 layer of the ionosphere, *J. Geophys. Res.*, *84*, 3360.

Torr, M., P. G. Richards, and D. G. Torr (1980), A new determination of the ultraviolet heating efficiency, *J. Geophys. Res.*, *85*(A12), 6819.

Weimer, D. R. (1995), Models of high-latitude electric potentials derived with a least error fit of spherical harmonic coefficients, *J. Geophys. Res.*, *100*, 19,595.

Woods, T. N., et al. (1998), TIMED solar EUV experiment, in *Missions to the Sun II*, edited by C. M. Korendyke, *Proc. SPIE Int. Soc. Opt. Eng.*, *3442*, 180–191.

Woods, T. N., F. G. Eparvier, J. Fontenla, J. Harder, G. Kopp, W. E. McClintock, G. Rottman, B. Smiley, and M. Snow (2004), Solar irradiance variability during the October 2003 solar storm period, *Geophys. Res. Lett.*, *31*, L10802, doi:10.1029/2004GL019571.

D. J. Pawlowski and A. J. Ridley, Department of Atmospheric, Oceanic and Space Sciences, University of Michigan, 2455 Hayward Street, Room 1424, Ann Arbor, MI 48109-2143, USA. (dpawlows@umich.edu)